Effects of artery size on the hydrodynamic diffusivity of red cells and other contained particles

Lydia I. Kolitsi and Stergios G. Yiantsios*
Department of Chemical Engineering, Aristotle University of Thessaloniki, University Box 453, GR 541 24, Thessaloniki, Greece

(Received 2 July 2019; published 26 November 2019)

Direct numerical simulations are presented for pressure-driven and simple shear channel flow of cell suspensions. The presence, motion, and deformation of cells are accounted for on the basis of the immersed interface method. Deformable microparticles are also included to model blood contained or pharmaceutical particles. The study focuses on the effects of channel height on the hydrodynamic diffusion characteristics of the contained particles. Although such effects are rather expected to be significant, they have not been systematically considered in the literature. The proximity with the bounding walls affects the mobility of the particles, even more so due to the low-Reynolds-number prevailing conditions. For pressure-driven flow the diffusivities increase with distance from the wall due to the increasing mobility and reach a channel-size-dependent maximum due to the diminishing local shear rate. Near the channel center, where the mean shear rates vanish, diffusivities remain finite owing to convection from cross-flow sweeps generated from the interaction of eddies formed in the opposing walls. It is suggested that the hydrodynamic mobility and its dependence on distance from the walls should be added to factors affecting the diffusivities, such as the local shear rate and the cell volume fraction and elasticity.

DOI: 10.1103/PhysRevFluids.4.113103

I. INTRODUCTION

Direct numerical simulations of blood flows are continually reaching increasing degrees of sophistication and faithfulness to the detailed mechanical, physiological, and other characteristics of the contained cells and the vascular networks [1–9]. Comprehending such flows and their correlation with cellular properties and interactions may contribute to valuable progress in the fundamental understanding of issues such as blood rheology [10–14], features manifested at the bifurcations of the circulatory network [15–17], transport of blood particles [18–25], manifestation of pathological conditions [26,27], and biomedical applications such as targeted drug delivery via the bloodstream [28–32]. Several important issues have been reviewed by Popel and Johnson [33] and more recently by Secomb [34], including rheological behavior, the hematocrit partition in bifurcations, and formation of a cell-free layer near artery walls.

In contrast to the formation of a cell-free layer by the dominant red cells, leukocytes and platelets tend to occupy the periphery of the cross-sectional lumen, and this property, commonly known as margination, is vital for the physiological responses of the immune system, inflammation and hemostasis. Since a typical target of said particles is the vascular walls, the predisposition for segregation toward the walls is a desirable characteristic that has received considerable attention [5,18–25]. A related issue of considerable importance and interest is the understanding and control of transport of pharmaceutical nano- and microparticles in the blood stream, which respond to

*yiantsio@auth.gr

similar types of stimuli, i.e., hydrodynamic forces and interactions mainly with the red blood cells (RBCs) [28–32]. Numerous simulation studies seek to shed light on the phenomena and mechanisms of margination of micro- and nanoparticles in blood flow in two and three dimensions (2D, 3D). Muller *et al.* [19] have demonstrated that 2D models can reproduce blood flow and particle margination characteristics in qualitative agreement with 3D models, yet they have limited capability of producing quantitative results accurate for 3D systems.

A widely adopted approach to describe the cross-flow distributions of RBCs, platelets, and other particles in a blood vessel is to introduce *diffusion* and *drift* terms in species balances [35]. Such distributions are governed by three types of mechanisms, namely, hydrodynamic "collisions" and fluctuations, hydrodynamic lift, and Brownian motion. In general, hydrodynamic diffusion is understood and modeled in terms of the concept of shear-induced diffusion introduced for rigid particle suspensions by Leighton and Acrivos [36]. Thus, a commonly proposed general expression for the diffusivities is [18,34]

$$\mathscr{D} \sim \gamma R^2 \phi f(\kappa), \tag{1}$$

where γ, R, ϕ are the shear rate, particle radius, and volume fraction, and $f(\kappa)$ contains the effects of cell membrane elasticity.

Crowl and Fogelson [37] employed the lattice Boltzmann method to study numerically the dispersion and margination of platelets in 2D blood suspensions flowing. The study was limited to a 50-μm channel. The detailed RBC and platelet trajectories obtained from the direct numerical simulations were used to obtain a diffusional flux with an almost constant diffusivity in the core flow region and a significant mean drift velocity in the wall vicinity, which for platelets points toward the wall in contrast to RBCs, thus expelling them into the cell-free layer. Zhao *et al.* [5] studied platelet margination during blood flow in a 3D channel and examined the effects of capillary number and hematocrit. The study was limited to a 34-μm channel. Simulations of the cross-flow particle migration in an RBC suspension undergoing bulk shear motion and a suspension flowing in a microchannel show a shear-induced diffusion and/or a mean lateral velocity, both due to hydrodynamic interactions between particles and RBCs. Three-dimensional numerical studies by Li *et al.* [31] in a cylindrical lumen demonstrated that both RBC-enhanced and Brownian diffusion are comparably important for rigid particles of diameter ~500 nm. Brownian diffusion, however, becomes the dominant mechanism for the dispersion of particles of diameter smaller than ~100 nm and is also proved to be significant for nanoparticle margination in venules. However, their study was limited to a single lumen diameter of 20 μm.

In the migration of RBCs away from the vessel wall, resulting in the formation of a cell-free layer, a dominant role is played by hydrodynamic lift, also termed deformability lift [23]. This lift is less significant for platelets and other rigid particles, and their cross-flow migration is mostly due to hydrodynamic interactions and collisions with RBCs. Relative rigidity is an important factor affecting the displacement of blood particles during collisions [18]. Crowl and Fogelson [37] attribute drift phenomena to the one-sided platelet-RBC collisions near the edge of the CFL, on the basis of which they also attempt to elucidate the sharp fluctuations they observed in the effective platelet lateral diffusion coefficient in the radial direction. The augmented platelet diffusion and drift due to their interaction with RBCs (RBC-enhanced diffusion) is, according to Vahidkhah *et al.* [20], a result of the local anisotropy in the RBC distribution. They suggest that the cellular microstructures formed by RBCs stacked along the wall-normal direction in a shear flow critically influence platelet margination, as they naturally render the instantaneous RBC distribution highly anisotropic by hydrodynamic forces creating local cavities in RBC distribution. These cavities can be used from platelets as an "express lane" for fast margination toward the wall.

A different approach from the diffusion-drift concepts of a more fundamental character has been introduced by Rivera *et al.* [22] and Qi and Shaqfeh [23,24]. More specifically, a kinetic-type theory was proposed to describe the distribution of particles on the basis of information for the displacement of pairs of RBCs colliding in a shear flow field. This information was obtained by simulating isolated pairs. Good agreement with experimental data has been obtained. Evidently,

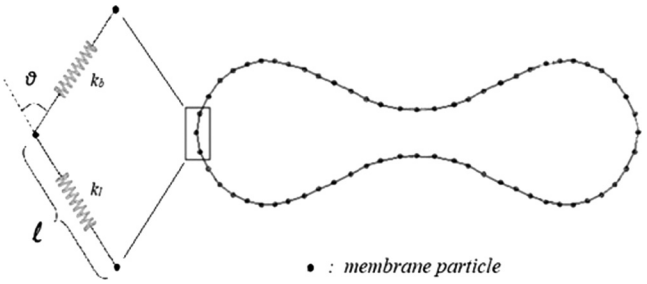

FIG. 1. The cell, considered as an assembly of nodes connected with elastic springs.

however, such an approach is limited to dilute suspensions, since under conditions of normal hematocrit it is unlikely that cells recover their shape, orientation, and equilibrium tank-treading motion before getting engaged in a new collision.

Although significant research has been conducted on the role of lumen diameter in blood rheology [6,10–14], the same cannot be said with regard to the diffusion processes of suspended blood particles. In view of all the above, the goal of the present work is to focus on the effect of the capillary artery size on particle diffusivity by investigating flow and particle transport via direct numerical simulations. For this purpose we consider pressure-driven and simple shear channel flows at fixed concentrations and capillary numbers and vary the channel height systematically. The simulations are in 2D, and therefore, as commented above, aim mostly at obtaining a qualitative understanding or semiquantitative description of the effects of vessel size rather than obtaining high-fidelity three-dimensional results.

The structure of the presentation is as follows: In Sec. II the mathematical model describing the elastic behavior of the cells and the fluid flow is outlined. Then, in Sec. III, the results of numerical simulations of flow in different channel heights are presented. Emphasis is placed upon the diffusion characteristics of red cells, microparticles, and tracers, which are quantified and commented. Finally, the main conclusions are summarized in Sec. IV.

II. GOVERNING EQUATIONS AND NUMERICAL METHODS

A. Overview

Each cell membrane is considered to be composed of a set of nodes, as shown in Fig. 1, representing the connection points between adjacent proteins, which are thought of as spring elements. Elastic forces act on each node due to the extension or compression of the proteins and the resistance of connections to bending. In 3D more features are added in order to obtain a faithful spring-based discrete analog of the cell membrane elasticity [38,39].

In our approach, the spring compression-extension elastic energy is expressed in the form [40,41]

$$E_s = \frac{1}{2} k_s \frac{(l - l_0)^2}{l_0^2}, \tag{2}$$

where k_s is an elastic constant, and l_0 and l are an equilibrium distance and the actual distance between nodes. Moreover, the springs attached to each node resist bending, and for this reason an additional contribution to the elastic energy exists in the form

$$E_b = \tfrac{1}{2} k_b \tan^2(\theta/2), \tag{3}$$

where k_b is a similar elastic constant and θ the angle between adjacent springs, as shown in Fig. 1. Finally, the total assembly of springs and nodes resists deformations that tend to modify its volume,

and this resistance is expressed in terms of a third elastic energy contribution of the form

$$E_v = \frac{1}{2} k_v \frac{(V - V_0)^2}{V_0^2}, \tag{4}$$

where k_v is another elastic constant and V_0 and V are the equilibrium and the actual cell volume. At any instant in time, given a configuration, the total force acting on node i is given by

$$\mathbf{F}_i = -\frac{\partial E}{\partial \mathbf{x}_i},$$

where E is the total elastic energy and $\mathbf{x}_i$ is the node position vector.

Now since the protein connecting nodes and the proteins themselves are considered to be entities of relatively small mass and hence small inertia also, the total elastic force acting on each node at any instance in time must be balanced by an equal-in-magnitude and opposite-in-direction hydrodynamic force. Then, from the principle of action and reaction a force equal to the elastic one is exerted on the fluid that surrounds the cells. Therefore the equation of momentum for the fluid, which is expressed in terms of the Navier-Stokes equations, is augmented by the elastic contribution from the immersed cells. This contribution is localized at the particular points in space where the cell nodes are instantaneously positioned. The force field acting on the fluid is therefore expressed in terms of a set of Dirac-delta functions distributed over the fluid domain. Then the governing equations for the fluid are the Navier-Stokes equations,

$$\rho\left(\frac{\partial \mathbf{u}}{\partial t} + \mathbf{u} \cdot \nabla \mathbf{u}\right) = -\nabla P + \mu \nabla^2 \mathbf{u} + \sum_i \mathbf{F}_i \delta(\mathbf{x}_i), \tag{5}$$

together with the continuity equation for an incompressible fluid,

$$\nabla \cdot \mathbf{u} = 0. \tag{6}$$

In some of the simulations microparticles were also added to the flow, at much lower concentrations than the red cells. These particles were also taken to be membrane-enclosed entities with the same elastic properties but with a volume corresponding to spheres with radius of 1 μm. Despite their deformability they remained nearly spherical during the flow.

In some of the simulations, interparticle forces were incorporated by employing a Morse-type potential between nodes of different particles [42]. Such forces originate from physicochemical interactions of van der Waals or osmotic nature, and their roles in the formation of rouleaux and on the rheological behavior at low shear rates are well known. However, for the level of shear rates employed in this work, the effects of such forces were negligible [11]. Lastly, it may be mentioned here that in some studies a different viscosity is attributed to the cell cytoplasm. However, this effect, which is not accounted for in the present formulation, does not lead to qualitatively different results [5,29].

B. Scaling and dimensionless parameters

A length scale L approximately equal to the diameter of a cell at equilibrium is adopted. This is taken here to be 10 μm. Then, given a shear rate γ_w, we may define a velocity scale as $U_0 = \gamma_w L$. Therefore, a cell Reynolds number for these flows is

$$\mathrm{Re} = \frac{\rho U_0 L}{\mu} = \frac{\rho \gamma_w L^2}{\mu}. \tag{7}$$

Since we consider properties of water for the pure fluid, this Reynolds number is numerically evaluated as $\mathrm{Re} = 10^{-4}\,\gamma_w$. For shear rates up to 1000 s^{-1} considered in this study the cell Reynolds numbers are much smaller than unity. Moreover, even on the basis of the channel thickness, the maximum Reynolds number does not exceed unity. Hence, the effects of inertia are neglected.

Scaling the pressure by $\mu U_0/L$ and the elastic force density by $k_s(L/l_0)^2/L^4$, the momentum equations are made dimensionless by dividing by the viscous term and writing

$$0 = -\nabla P + \nabla^2 \mathbf{u} + \frac{k_s(L/l_0)^2}{\mu\gamma L^3} \sum_i \hat{\mathbf{F}}_i \delta(\hat{\mathbf{x}}_i) \tag{8}$$

or

$$0 = -\nabla P + \nabla^2 \mathbf{u} + \frac{1}{Ca} \sum_i \hat{\mathbf{F}}_i \delta(\hat{\mathbf{x}}_i). \tag{9}$$

Thus, a dimensionless parameter in the form of a capillary number appears, defined as

$$Ca = \frac{\mu\gamma_w L^3}{k_s(L/l_0)^2}, \tag{10}$$

which expresses the ratio between viscous forces tending to deform the cells and elastic forces tending to restore their shape. An estimate of this parameter may be obtained as follows. From Pivkin and Karniadakis [39] we have the expression

$$k_s \sim \frac{k_B T l_{\max}}{4p}, \tag{11}$$

where k_B is the Boltzmann constant, equal to 1.38×10^{-23} J/K, $l_{\max}$ is the maximum stretched length of the proteins equal to $3.7l_0$, where $l_0 = 75$ nm, and p is a persistence length, equal to 7.5 nm. Therefore the parameter Ca is estimated to be $Ca \sim 10^{-3}\,\gamma_w$. The bending stiffness and volume conservation parameters, k_b,k_v, were taken equal to k_s and $100\,k_b$, respectively [41].

C. Numerical method

A numerical approach based on the Galerkin finite element method was adopted. The approach is a simplified variant of a methodology known as *distributed Lagrange multiplier/fictitious domain method* (DLM/FDM), developed for the direct numerical simulation of particle-laden multiphase flows and flows containing moving solids by Glowinski *et al.* [43–45]. In this respect, the applied forces are treated in a similar fashion as the Lagrange multipliers employed to enforce the motion of the solid bodies in the DLM/FDM. However, the approach is simpler because the immersed cells are assumed to have no inertia. This has been implemented in Glowinski *et al.* [41]. Accordingly, the weak formulation of the momentum equations becomes

$$\int_\Omega \nabla \mathbf{u} \cdot \nabla \mathbf{v} d\mathbf{r} = \int_\Omega p \nabla \cdot \mathbf{v} d\mathbf{r} + \frac{1}{Ca} \int_\Omega \sum_i \hat{\mathbf{F}}_i \delta(\hat{\mathbf{x}}_i) \cdot \mathbf{v} d\mathbf{r}, \tag{12}$$

where $\boldsymbol{v}$ is a function from the velocity test space, and $\hat{\mathbf{F}}_i$ are the elastic forces on the nodes, determined from their relative positions, as discussed already. The incompressibility condition, applied over the whole domain, Ω, is

$$\int_\Omega q \nabla \cdot \mathbf{u} d\mathbf{r} = 0, \;\; \forall q \in L^2(\Omega), \tag{13}$$

where q belongs to the pressure function test space. Velocities were represented by biquadratic shape functions within the elements (quadratic in each spatial direction). On the other hand, a discontinuous representation of pressure within each element (Crouzeix-Raviart elements) was employed. In the numerical implementation, a coupled iterative Uzawa method was employed for the velocity and pressure based on the conjugate gradient method [46,47]. At each time step of the transient simulations, after obtaining the velocity field the node positions were advanced by an explicit scheme where the time step was limited by the cell stiffness. A spatially uniform grid was employed, with ten nodal points per dimensionless unit length. Such a resolution was deemed

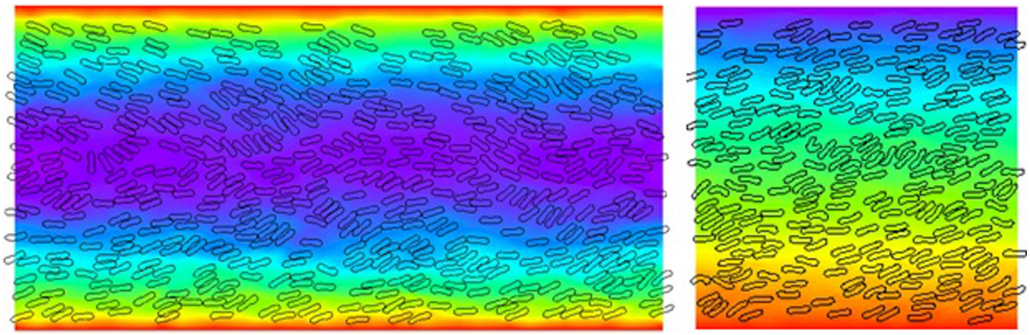

FIG. 2. Snapshots of instantaneous streamwise velocity, represented in an arbitrary chromatic scale, and the positions of cells for pressure-driven (left) and simple shear flow (right).

adequate on the basis of numerical tests where the resolution was increased to 15 points per unit length.

III. RESULTS AND DISCUSSION

Transient simulations of pressure-driven flow have been performed for several different channel heights, namely, 20, 40, 80, 120, 160, and 200 μm. The number of cells in the flow channels was adjusted to keep an area fraction for the cells of 30%. To keep the same wall shear rate γ_w, for all channels the constant pressure drop applied was given by

$$\frac{\Delta P}{L} = \frac{2\mu\gamma_w}{H}, \tag{14}$$

where μ is the pure fluid viscosity and H the channel height. In addition, simulations of simple shear flow between parallel plates were performed for similar cell volume fractions by imposing opposite velocities on the plates. The plate distances were 30, 60, 90, and 120 μm, and the nominal shear rate was fixed by setting their velocities equal to $\pm\gamma_w H/2$. For the pressure-driven flow the wall shear rate was set equal to 200 s^{-1}, roughly representative of the conditions in capillary arteries. Some shear flow simulations were performed at the same nominal shear rate, whereas a few more were performed at 1000 s^{-1} for computer time economy, since the shear rate is inversely related to the numerical time step. All the channels had a finite length, and periodic conditions were imposed along the flow direction. In all simulations the length was at least equal to the height, and in some it was twice or three times that value.

A. Qualitative and mean flow characteristics

A sample of an instantaneous field with color contours of streamwise velocity together with the distribution of cells and microparticles is shown on Fig. 2 (left). Larger velocities prevail near the channel center, and the presence of cells results in a blunted profile approaching a plug, whereas higher shear rates prevail near the channel walls. The orientation of the cells may be observed to adjust to the shear rate near the walls, indicating a tank-treading type of motion for their membranes. On the other hand, near the center, where the shear rates are lower, the orientation of cells is more random. A representative similar picture from the shear flow simulations is shown in Fig. 2 (right).

In contrast to the pressure-driven flow case, in pure shear the orientation of the cells was found to be more uniform over the entire flow domain. This may be obtained from the principal directions of the moment of inertia tensor of the cells [2]. For all channel heights, the average angle of inclination was similar and equal to about 16°, in interesting accord with literature values from 3D simulations of red cells in simple shear flow [5].

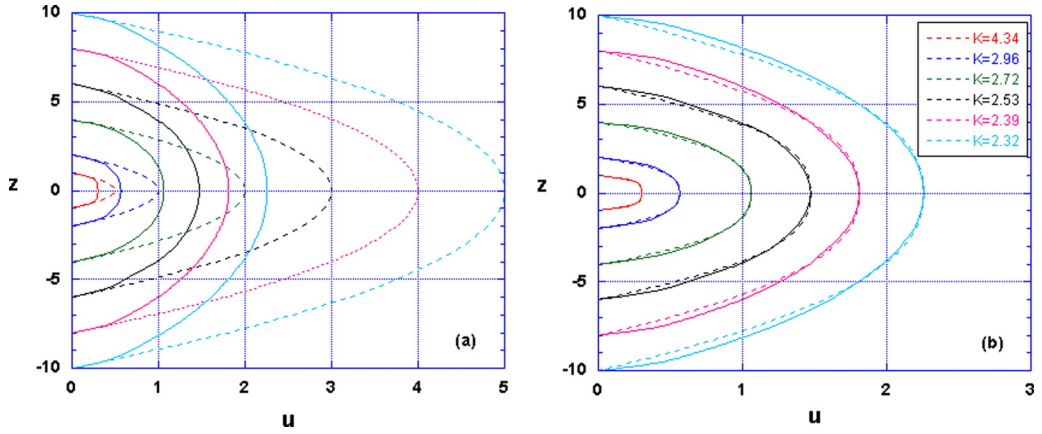

FIG. 3. Average streamwise velocity distributions for all channel sizes in the pressure-driven flow simulations. All cases share the same wall shear stress. (a) The dotted lines show the parabolic profiles for a cell-free fluid. (b) Data fitted according to expression (15). The vertical coordinate z is scaled with the common length scale taken to be 10 μm.

More quantitative information on the velocity fields for the pressure-driven flows is presented in Fig. 3(a), where the time-averaged streamwise velocity for all the simulated channel heights is shown as a function of position between the bounding walls. Here, vertical distances are scaled with the reference scale of 10 μm, a length close to the diameter of a cell, as discussed in the previous section. The blunting of the profiles is evident, especially for the narrower channels. Superimposed to these profiles are the theoretical ones which correspond to the flow of a cell-free fluid. It may be observed that the profiles match near the walls, since the shear rates are identical and these regions are relatively depleted from cells. The deviations start at some distance from the walls due to the presence of cells, which are the cause of blunting of the profiles.

Lastly, in Fig. 3(b) the same data are fitted through expressions of the form

$$u = u_{\max}\left[1 - \left(\frac{z}{H/2}\right)^{K}\right], \tag{15}$$

frequently used in the literature [28,30,33]. The exponents, shown in the legend, increasingly deviate from the value of 2 as the channels become narrower.

Mean flow profiles for the shear flows for all the simulated channels are shown in Fig. 4. Similar levels of shear prevail over most of the flow domain for all cases. The shear rates are higher in the regions adjacent to the walls, because these regions are relatively depleted of cells.

We note parenthetically that on the basis of the comparison between pure fluid and cell-suspension flow rates an apparent viscosity may be obtained. Interestingly, despite the 2D nature of the simulations, the results compare very favorably with the empirical relation proposed by Pries *et al.* [48], which correlates viscosity with hematocrit and tube diameter on the basis of experimental data of blood flow in glass tubes.

Cell concentration distributions, again time-averaged, are shown in Fig. 5 for some of the pressure-driven simulations. As the channel height increases, the concentration profiles become more uniform, whereas nonuniformities are more pronounced in the smaller channels. In all cases a cell-free layer on the order of a few microns is also apparent in the vicinity of the walls. The size of this layer has been suggested to be dictated by the magnitude of wall shear, bulk concentration, and cell elasticity [27].

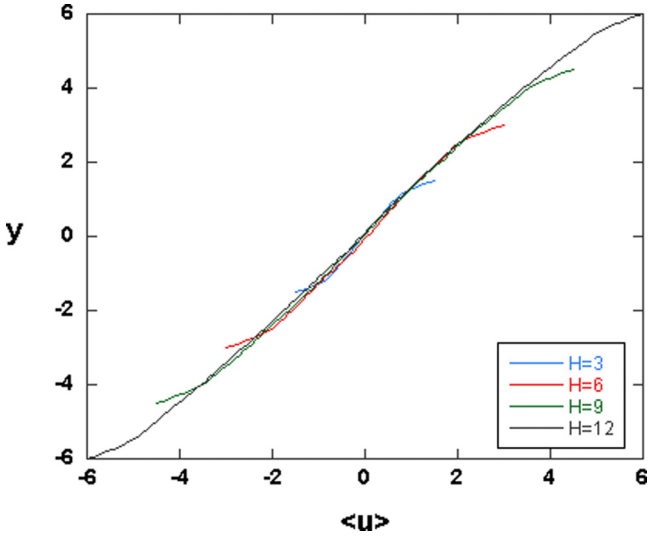

FIG. 4. Average streamwise velocity distributions for all channel sizes in the shear flow simulations.

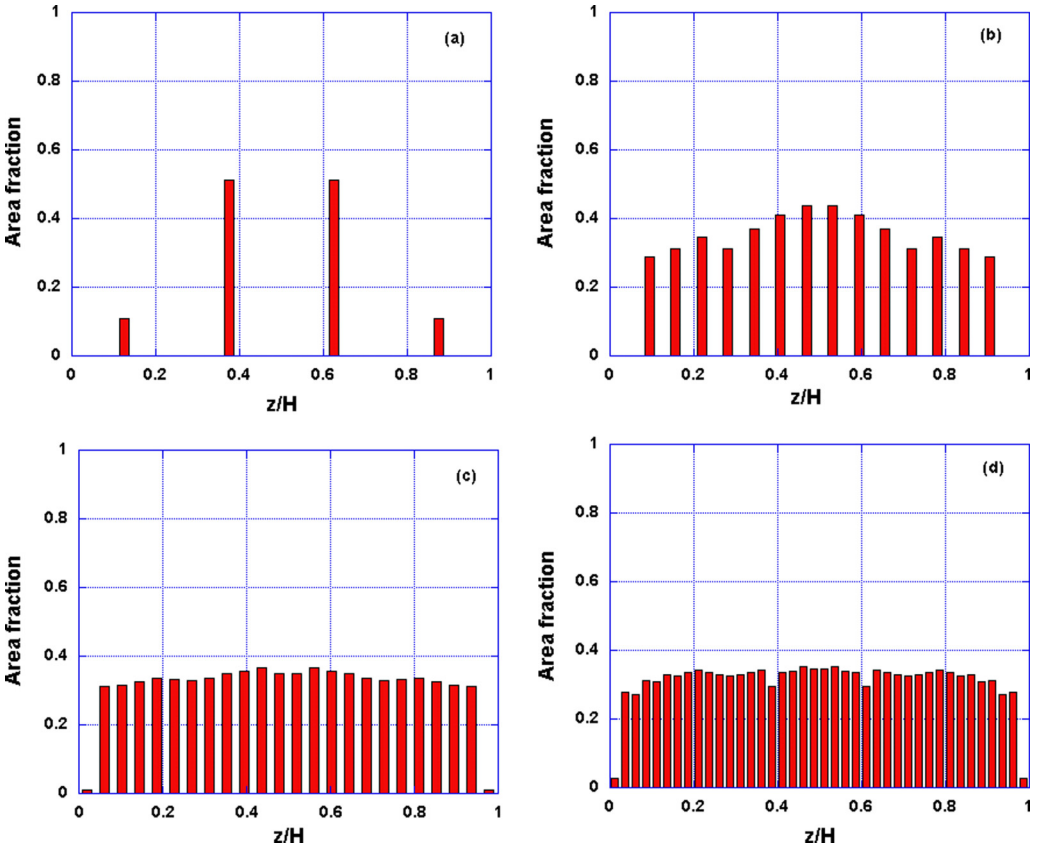

FIG. 5. Cell concentration distributions in the pressure-driven flow simulations for various dimensionless channel heights: (a) $H = 2$, (b) $H = 8$, (c) $H = 12$, and (d) $H = 20$.

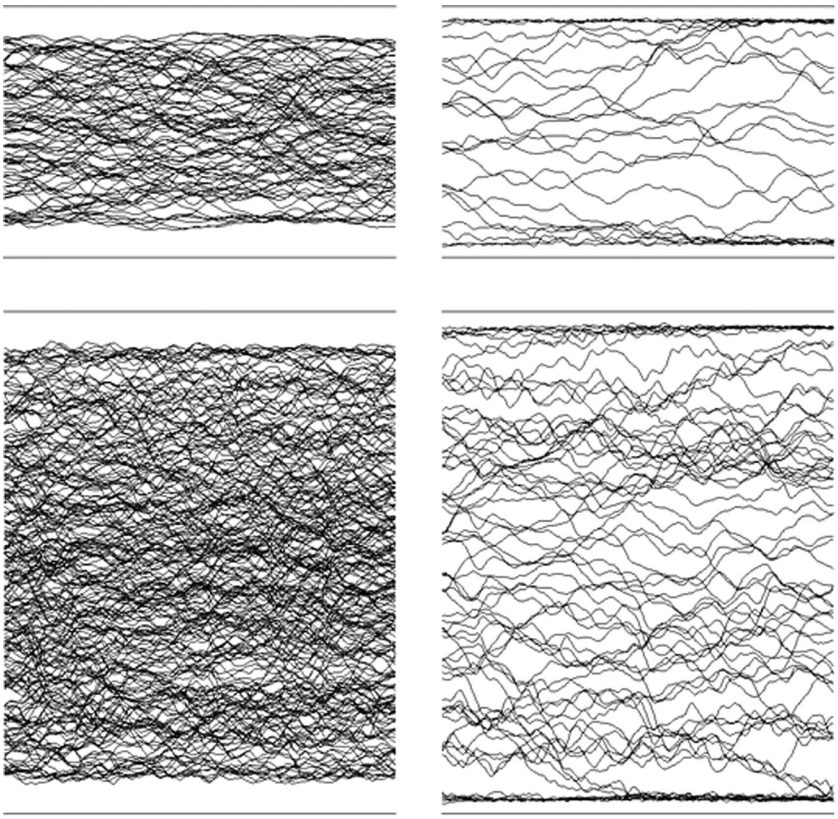

FIG. 6. Trajectories of red cells (left) and microparticles (right) in the form of their vertical position in the channel as a function of time. The horizontal axis represents time over a frame of 200 dimensionless units. The top and bottom rows are for channels with dimensionless heights 4 and 8, respectively. The phenomenon of margination is evident in the microparticle trajectories.

B. Shear-induced diffusion

We next turn to the transient characteristics of the individual motions of cells and particles. In the same manner as presented by Crowl and Fogelson [37], cell and particle trajectories are shown in Fig. 6 for some of the pressure-driven channel flow simulations. These trajectories are presented in the form of instantaneous vertical position versus time. Again, a first observation is the development of the cell-free layer. A second one is the tendency of the microparticles to gradually become trapped and collect in the cell-free layer. Thus, the phenomenon of margination is manifested in the present simulations.

As discussed in the Introduction, from a macroscopic point of view the randomness of cell motion and the development of the cell-free layer may be described as the combined result of two processes: a diffusion process together with drift away from the walls. The first may be viewed as the result of collisions between cells which move past each other due to their different longitudinal velocities and are consequently mutually displaced. Hence, the level of shear at different distances from the walls plays a determining role. The drift process is the result of hydrodynamic interactions of the soft particles with the bounding walls and is mainly limited to the vicinity of the walls.

Quantitative information on these two processes may be obtained from the trajectory data in a similar manner as in Crowl and Fogelson [37] and Li *et al.* [31]. Since concentrations and shear rates vary with distance from the walls, evidently the shear-induced diffusion coefficients and the drift

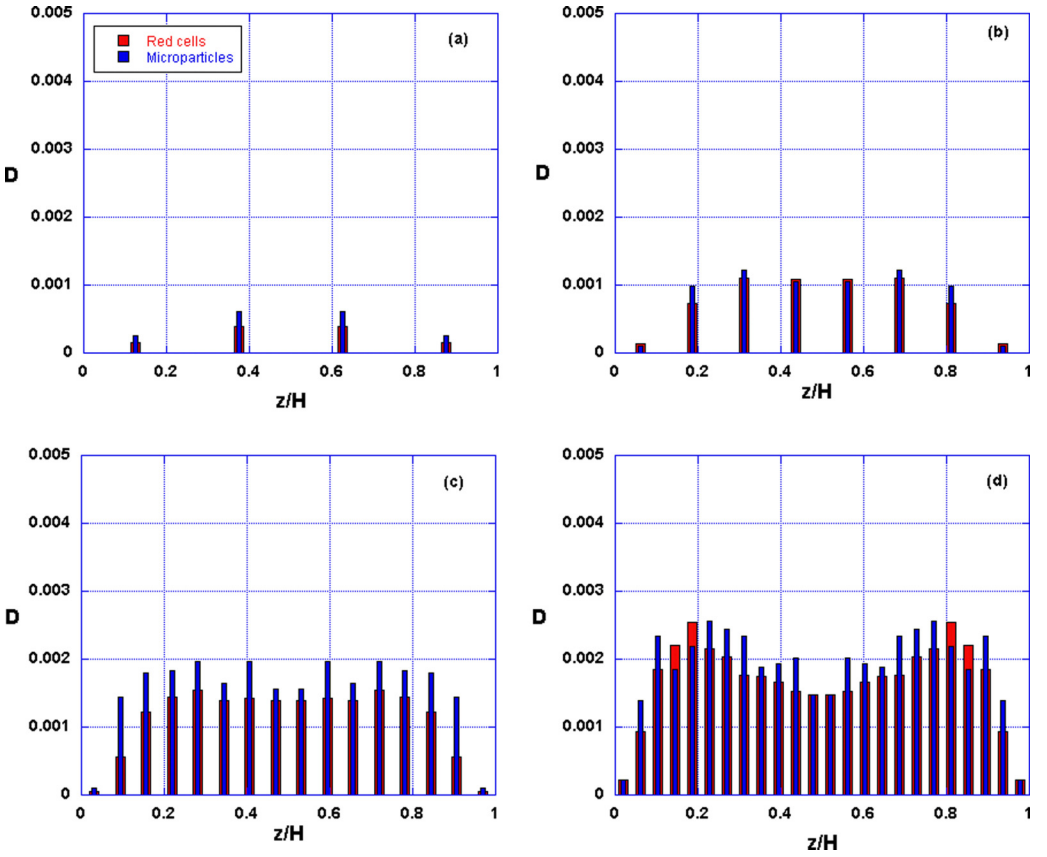

FIG. 7. Diffusivities of cells and microparticles in the pressure-driven flow simulations for various dimensionless channel heights: (a) $H = 2$, (b) $H = 4$, (c) $H = 8$, and (d) $H = 12$.

velocities must depend on this distance, in addition to other factors such as the average concentration and the channel height. For this reason, the channels were divided in sections of thickness equal to 5 μm, and separate averaging was applied to obtain individual values for each section. Drift velocities and diffusivities were obtained here by time-averaging data on the displacements through the expressions

$$u_{\text{drift}} = \frac{\langle z(t + \Delta t) - z(t) \rangle}{\Delta t} \tag{16}$$

$$\mathscr{D} = \frac{\langle [z(t + \Delta t) - u_{\text{drift}} \Delta t - z(t)]^2 \rangle}{2\Delta t}. \tag{17}$$

The obtained results were not sensitive to the precise value of the time interval Δt, as long as it was larger than several time units $({\gamma_w}^{-1})$.

We first focus on the diffusion coefficients, which is the main theme of the present work. In Fig. 7 results are shown for cell and microparticle diffusivities in several of the simulated channels. The values presented are dimensionless, naturally scaled by $\gamma_w L^2$, as is usually proposed in the literature [18,34].

In several simulations, trajectories of tracer points moving with the fluid, either outside or inside the cells, were recorded. On the basis of such data a comparison between cell and tracer diffusivities may be obtained as shown in Fig. 8.

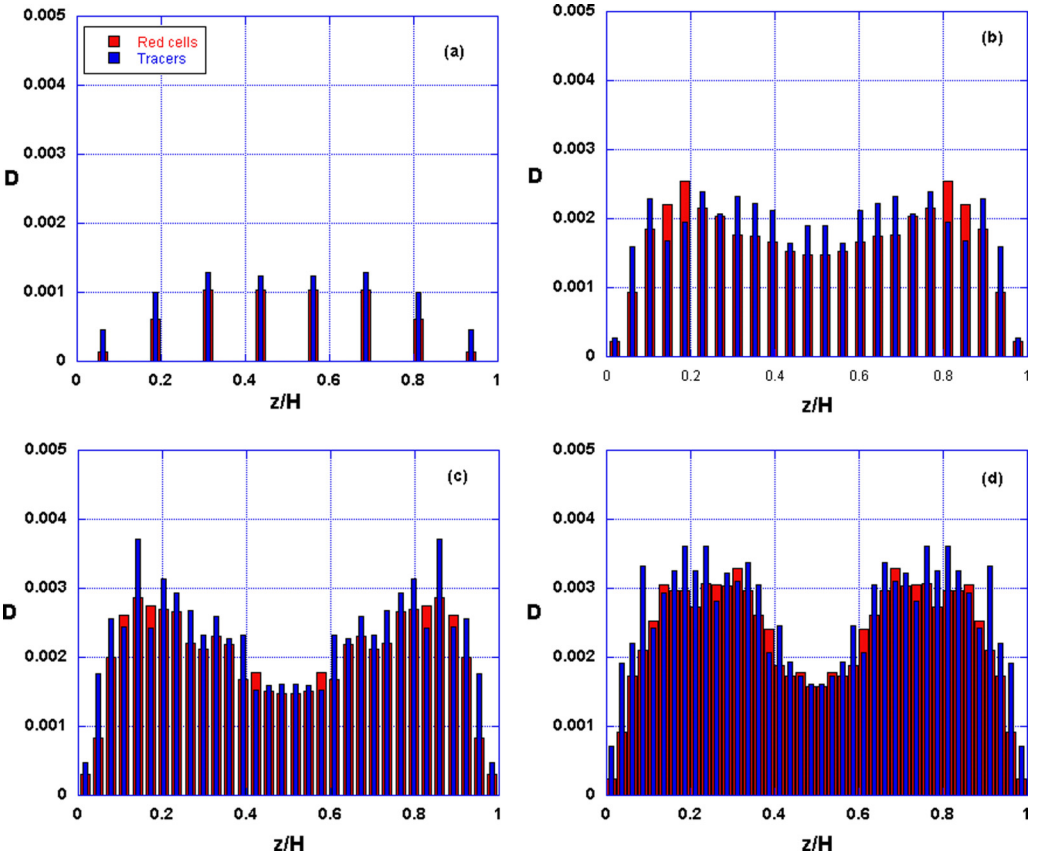

FIG. 8. Diffusivities of cells and tracers in the pressure-driven flow simulations for various dimensionless channel heights: (a) $H = 4$, (b) $H = 12$, (c) $H = 16$, and (d) $H = 20$.

It is evident that diffusivities of immersed microparticles and tracers are similar in magnitude to those of the cells. This is reasonable, since the cells constitute the majority of suspended species, and their interactions determine the velocity perturbations that characterize the dispersion [22,37]. A second observation is that diffusivities clearly depend on channel height and manifest an overall increase with it. A third observation is the clear dependence of the diffusivities on position in the channel. In particular, these diffusivities tend to increase with distance from the wall due to diminishing hydrodynamic wall limitations and, especially for the larger channels, to reach a maximum away from the channel center, where the prevailing shear rates vanish.

To further inquire into the observed behavior, in Fig. 9 we show snapshots of perturbation velocity fields in the form of velocity vectors obtained by subtracting the streamwise spatially averaged values from the instantaneous fields. It may be observed that the major activity in the form of eddies is located near the walls, where the higher shear rates prevailing lead to more frequent collisions between the cells. This region of activity as well as the size of eddies becomes larger as the channel height becomes larger. On the other hand, the channel center is a relatively quiescent region due to the low shear rates there. However, still some perturbations may be observed, with large-scale sweeps covering the whole central area and leading to coordinated motion from one wall region to the other. Thus it appears that the disturbance motion in the central area is due to the interactions of eddies generated from the two separate walls.

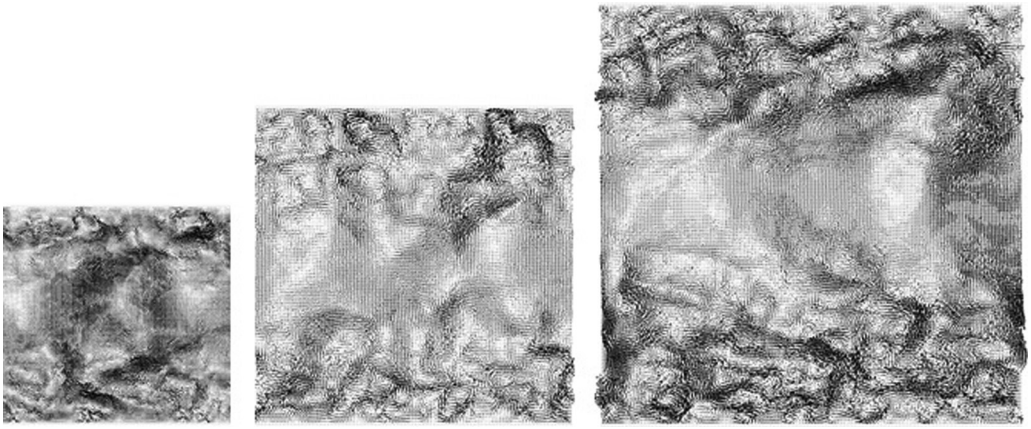

FIG. 9. Instantaneous disturbance velocity fields from the pressure-driven flow simulations showing the eddies near the walls and the large-scale sweeps near the channel center for channel heights: $H = 8$, 12, and 16.

To corroborate the above qualitative observations, in Fig. 10(a) are shown samples of wall-normal velocity two-point correlations for separations Δx along the flow direction, obtained from expressions of the form

$$R_{ww}(\Delta x, z) = \frac{\langle w(x_0, z)w(x_0 + \Delta x, z)\rangle}{\langle w(x_0, z)w(x_0, z)\rangle}, \tag{18}$$

by averaging over the streamwise reference locations x_0, as well as over time. Such functions are related to the size of eddies at different distances from the wall. It is clear from their shape that the size of eddies increases with distance from the wall and approaches dimensions of the order of the blunted profile flow region in the channel center. In Fig. 10(b) is also shown a comparison of the correlations for different channels at the same distance close to the wall. It is evident that near the wall all the correlations are roughly similar, which suggests that the local shear rate and the distance from the wall are the dominant factors.

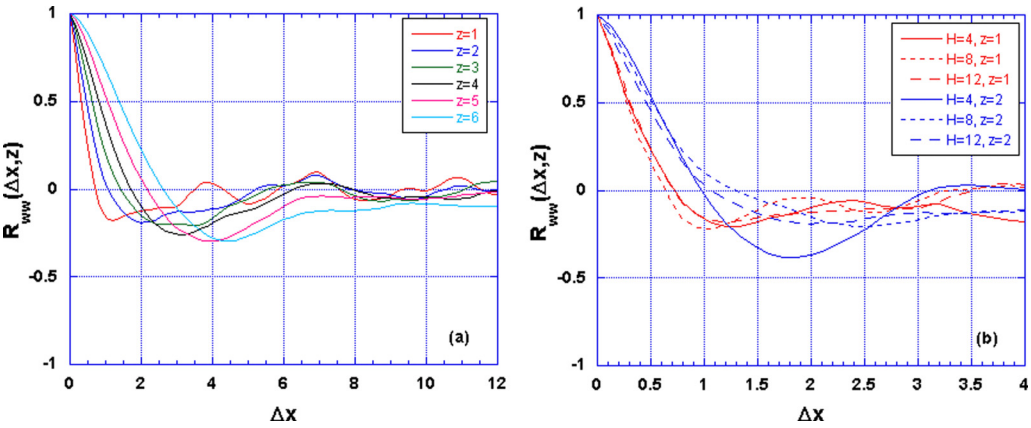

FIG. 10. Two-point velocity correlation functions as functions of distance in the streamwise direction for various positions across the channel, shown in the captions: (a) $H = 12$ and (b) the same functions for different channel heights, indicated in the legend.

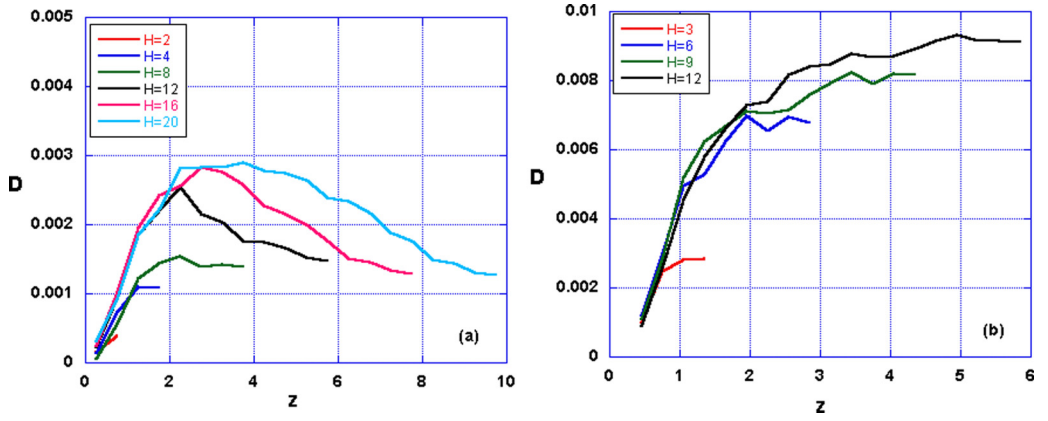

FIG. 11. Diffusivities as functions of the uniformly scaled distance from the wall for all channel heights: (a) pressure-driven flows and (b) shear flows.

In view of all the above, it becomes evident that the overall picture of the diffusivities may be better presented if the diffusivities are plotted as functions of the distance from the channel wall scaled with a common length scale for all channels (i.e., the red cell diameter) rather than with the individual height of each channel. This is done in Fig. 11(a), where the results from the simulations for all channels are presented. Indeed, a degree of data collapse is obtained in this manner. In particular, near the wall all curves appear to overlap, perhaps with the exception of the smaller channel, which is only two diameters wide. An increasing maximum at an increasing distance is also apparent as a result of the local shear rate being reduced with distance. One additional feature is that near the center, where the shear rate is very small, a finite diffusivity is obtained. A similar picture is obtained from the data of the shear flow simulations. Again, the data tend to overlap, perhaps with the exception of the smallest channel. Since the shear rate tends to a constant value, a maximum is not observed with distance but instead, the diffusivities tend to increase monotonically.

The above behavior suggests that three factors play a role in determining the overall behavior. First of all, the magnitude of the local shear rate determines the frequency of collisions and therefore is expected to directly influence the magnitude of the diffusivities through a scaling of the form γL^2.

A second factor is hydrodynamic wall interactions, which limit the ease of the colliding cells to deviate from their trajectories. In particular, the lower values for the narrower channel point to the fact that even the interactions with the more distant wall should be important. One may account for these interactions by evaluating the mobility of a particle near a solid surface. In two-dimensional geometry the mobility m of a disk of radius r toward a wall is given by Jeffrey and Onishi [49] as

$$\frac{m}{4\pi\mu} = \log\left[\frac{d + (d^2 - r^2)^{1/2}}{r}\right] - \frac{(d^2 - r^2)^{1/2}}{d}, \tag{19}$$

where d is the distance from the wall and μ the fluid viscosity. This could be an acceptable approximation for all but the narrowest channel, since at the channel center it gives an asymptotic expression of the form

$$\frac{m}{4\pi\mu} = \log\left(\frac{d}{r}\right) - 0.31 + O\left(\frac{r}{d}\right), \tag{20}$$

whereas the result accounting for both walls is (cf. Happel and Brenner [50], p. 345)

$$\frac{m}{4\pi\mu} = \log\left(\frac{d}{r}\right) - 0.62 + O\left(\frac{r}{d}\right). \tag{21}$$

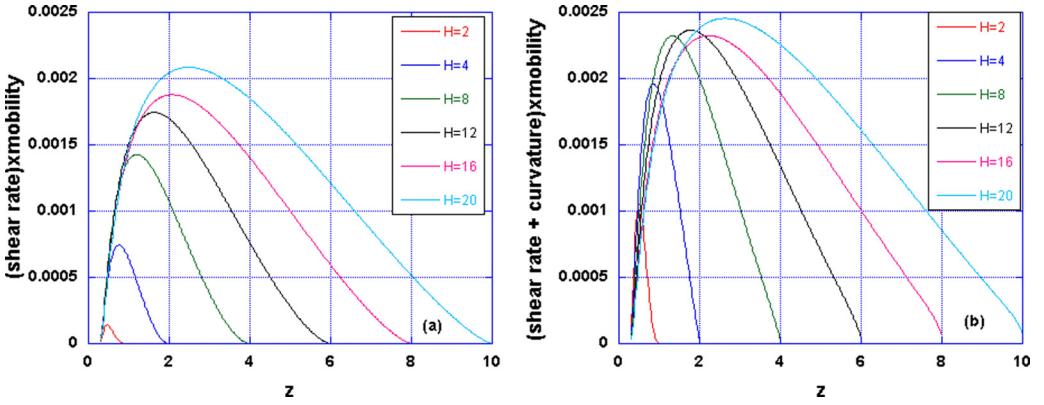

FIG. 12. (a) Local mean shear rate multiplied by the particle mobility for all channels in the pressure-driven flows. (b) The sum of local shear rate and flow curvature multiplied by the particle mobility.

In order to better represent the data in the vicinity of the channel center, Eq. (19) was modified to yield values that fitted well the results of Dvinsky and Popel [51], who performed numerical simulations for disks moving in 2D channels and presented the resistance functions in graphical form. Of course, a 2D cell is still different from a disk, but as a first approach and in a semiquantitative spirit, this should be sufficient for our purposes.

Now, if one prepared a plot of the product of the local shear rate, based on the mean flow fields, with the mobility factor as a function of distance from the wall, several features of the observed behavior for the diffusivities would be captured. This is seen in Fig. 12(a). In particular, the curves tend to overlap near the wall for all but the smallest channel, where the distant wall effects are important. A maximum is also captured due to the competition between logarithmically increasing mobility and the algebraically diminishing shear rate away from the wall. However, all the curves return to zero at the channel center because the shear rate is zero there. To account for this deficiency, following Nott and Brady [52] and their suggestion of the concept of a nonzero suspension temperature, a constant factor may be added to the local shear rate [23,24,53]. On the other hand, Rivera *et al.* [22] suggest that an additional factor that may account for finite diffusivities is the curvature of the flow. However, as may be seen in Fig. 12(b), if a term proportional to the curvature of velocity profile is added its effect turns out to be more pronounced near the walls rather than near the center.

Thus, here the solid lines presented in Fig. 13(a) to fit the data from the numerical simulations were obtained by adding constant terms to the local shear rate. These constant terms were 0.26, 0.23, 0.18, 0.16, 0.14, and 0.13, respectively, in going from the smaller to the larger channel. The same expressions but without the additional constant shear term and without any other fitting parameter were also used to obtain the solid lines in Fig. 13(b) for the shear flow simulations. It is suggested that the agreement between the numerical results and the simple expression is encouraging and lends credence to the proposed mechanisms.

Finally, considering the results on diffusivities and flow fields combined, it may appear plausible that the third factor playing a role in the characteristics of diffusion near the channel center is the interaction of eddies originating from the two opposing walls, which cause large-scale transverse motions across the channel center and the transport of cells and microparticles with them, as schematically suggested in Fig. 14. Then it may be plausible that near the center the diffusivities scale with the shear rate and the mobility at some distance from the wall.

Lastly, we briefly comment on the issue drift velocity, which, however, is not within the focus of the present work. Several references provide detailed information on mechanisms and quantitative force and drift velocity predictions in shear flows near walls, mostly for isolated vesicles [54–59].

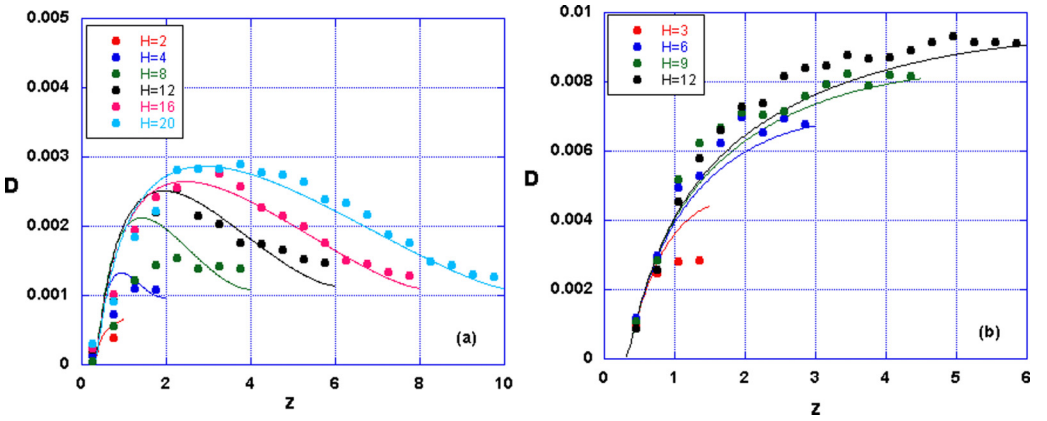

FIG. 13. Fitting of the diffusivity for (a) pressure-driven flows and (b) shear flows.

Drift velocities are shown in Fig. 15 as a function of distance from the wall for various channel heights. Despite the scatter it is apparent that all the curves appear to overlap, since drift is limited to a relatively short distance from the wall and is negligible further away in the bulk. It is thus determined by the details over the cell-free layer and the shear rate near the wall, which is similar for all channels. The results from the simple shear simulations at the same shear rate, shown with open circles, are in quantitative agreement with this behavior. A small difference with shear results at a rate of $1000\,\mathrm{s}^{-1}$ may be attributed to the higher capillary number and hence the higher deformability lift. An expression of the form $u_{\mathrm{drift}} \sim \gamma/z$ is frequently employed in the literature to describe the drift velocity as a function of the distance z from the wall [23,24,35]. It appears that the present data, despite their scatter, conform to such a relation, as seen by the dashed lines.

IV. SUMMARY AND CONCLUDING REMARKS

Direct numerical simulations of blood flows were performed in prototype geometries under conditions of pressure-driven and simple shear flow. The cells were represented as capsules with massless elastic membranes possessing shear and bending resistances. Deformable microparticles were also included in some of the simulations to represent blood contained or pharmaceutical particles. Despite the two-dimensional character of the simulations, encouraging results were obtained in terms of mean flow characteristics, such as the velocity distributions, the formation of the near-wall cell-free layer, the viscosity of the suspensions, and the tendency of the microparticles for margination.

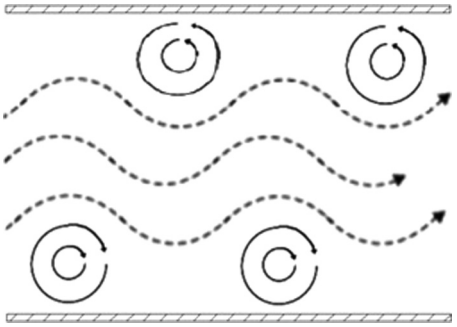

FIG. 14. Qualitative sketch of the wall-generated eddies and their role in producing the upward and downward sweeps in the middle of the channel.

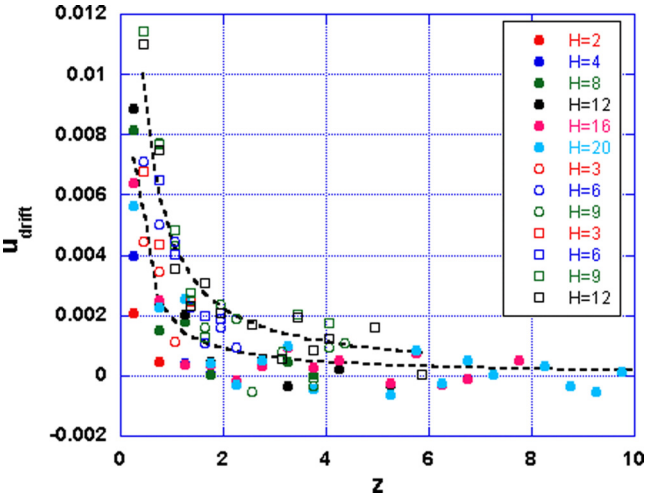

FIG. 15. Cells drift velocities away from the wall as functions of the uniformly scaled distance for all channel heights. Closed symbols represent pressure-driven flows and open ones shear flows. Circles are for a shear rate of 200 s^{-1} and squares for 1000 s^{-1}.

The study focused on the dispersion characteristics of contained particles. Their shear-induced diffusivities are determined by the cells, since they represent the major contained species and depend on several factors, including the local shear rate, particle concentration, and their elasticity. Channel height was systematically varied, and it was shown that this has a rather expected significant effect, since the proximity with the bounding walls affects the mobility of the particles, even more so due to the low-Reynolds-number prevailing conditions.

In the pressure-driven flow simulations, which are more relevant to blood flow, the diffusivities increase with distance from the wall due to the increasing mobility and exhibit significant data overlapping for different channel sizes, since the near-wall shear rates are common. Diffusivities reach a channel-size-dependent maximum due to the diminishing local shear rate. Although mobility effects are more pronounced in the 2D simulations performed here, it is expected that they will be significant also in the more realistic 3D cases, especially for channel dimensions that are less than 100 μm.

It is thus suggested that the hydrodynamic mobility m and its dependence on distance from the walls should be considered and included in the functional dependence of the diffusivities in a form of the type $\mathscr{D} \sim \gamma R^2 m\phi f(\kappa)$. Near the channel center, where the mean shear rates vanish, diffusivities remain finite owing to convection from cross-flow sweeps that are generated from the interaction of eddies formed near the opposing walls. On the other hand, the effects of the curvature of the mean flow profile appear to be minor. All the above considerations might be helpful in the development of simplified models for pharmaceutical particle transport based on continuum concepts and convention-diffusion descriptions for the contained species.

ACKNOWLEDGMENTS

Partial support of this work is acknowledged by the European Union and Greek national funds through the Operational Program Competitiveness, Entrepreneurship and Innovation program, under the call RESEARCH – CREATE – INNOVATE (Project Code No. T1EDK-02775).

[1] C. Pozrikidis, *Computational Hydrodynamics of Capsules and Biological Cells* (CRC Press, Boca Raton, FL, 2010).

[2] S. Ramanujan and C. Pozrikidis, Deformation of liquid capsules enclosed by elastic membranes in simple shear flow: Large deformations and the effect of fluid viscosities, J. Fluid Mech. **361**, 117 (1998).
[3] C. K. Aidun and J. R. Clausen, Lattice-Boltzmann method for complex flows, Annu. Rev. Fluid Mech. **42**, 439 (2010).
[4] D. A. Reasor, Jr., J. R. Clausen, and C. K. Aidun, Coupling the lattice-Boltzmann and spectrin-link methods for the direct numerical simulation of cellular blood flow, Int. J. Numer. Meth. Fluids. **68**, 767 (2011).
[5] H. Zhao, E. S. G. Shaqfeh, and V. Narsimhan, Shear-induced particle migration and margination in a cellular suspension, Phys. Fluids **24**, 011902 (2012).
[6] H. Lei, D. A. Fedosov, B. Caswell, and G. E. Karniadakis, Blood flow in small tubes: Quantifying the transition to the non-continuum regime, J. Fluid Mech. **722**, 214 (2013).
[7] X. Li, Z. Peng, H. Lei, M. Dao, and G. E. Karniadakis, Probing red blood cell mechanics, rheology and dynamics with a two-component multi-scale model, Philos. Trans. R. Soc. London, Ser. A **372**, 20130389 (2014).
[8] T. Krüger, *Computer Simulation Study of Collective Phenomena in Dense Suspensions of Red Blood Cells under Shear* (Springer, New York, 2012).
[9] P. Balogh and P. Bagchi, A computational approach to modeling cellular-scale blood flow in complex geometry, J. Comput. Phys. **334**, 280 (2017).
[10] W. Pan, D. A. Fedosov, B. Caswell, and G. E. Karniadakis, Predicting dynamics and rheology of blood flow: A comparative study of multiscale and low-dimensional models of red blood cells, Microvasc. Res. **82**, 163 (2011).
[11] D. A. Fedosov, W. Pan, B. Caswell, G. Gompper, and G. E. Karniadakis, Predicting human blood viscosity in silico, Proc. Natl. Acad. Sci. USA **108**, 11772 (2011).
[12] D. A. Fedosov, H. Noguchi, and G. Gompper, Multiscale modeling of blood flow: From single cells to blood rheology, Biomech. Model. Mechanobiol. **13**, 239 (2014).
[13] M. Gross, T. Kruger, and F. Varnik, Rheology of dense suspensions of elastic capsules: Normal stresses, yield stress, jamming and confinement effects, Soft Matter **10**, 4360 (2014).
[14] A. Yazdani, X. Li, and G. E. Karniadakis, Dynamic and rheological properties of soft biological cell suspensions, Rheol. Acta. **55**, 433 (2016).
[15] C. Bacher, L. Schrack, and S. Gekle, Clustering of microscopic particles in constricted blood flow, Phys. Fluids **2**, 013102 (2017).
[16] P. Balogh and P. Bagchi, Analysis of red blood cell partitioning at bifurcations in simulated microvascular networks, Phys. Fluids **30**, 051902 (2018).
[17] T. Ye and L. Peng, Motion, deformation, and aggregation of multiple red blood cells in three-dimensional microvessel bifurcations, Phys. Fluids **31**, 021903 (2019).
[18] A. Kumar and M. D. Graham, Segregation by membrane rigidity in flowing binary suspensions of elastic capsules, Phys. Rev. E **84**, 066316 (2011).
[19] K. Muller, D. A. Fedosov, and G. Gompper, Margination of micro- and nano-particles in blood flow and its effect on drug delivery, Sci. Rep. **4**, 4871 (2014).
[20] K. Vahidkhah, S. L. Diamond, and P. Bagchi, Platelet dynamics in three-dimensional simulation of whole blood, Biophys. J. **106**, 2529 (2014).
[21] T. Kruger, Effect of tube diameter and capillary number on platelet margination and near-wall dynamics, Rheol. Acta. **55**, 511 (2016).
[22] R. G. H. Rivera, X. Zhang, and M. D. Graham, Mechanistic theory of margination and flow-induced segregation in confined multicomponent suspensions: Simple shear and Poiseuille flows, Phys. Rev. Fluids **1**, 060501 (2016).
[23] Q. M. Qi and E. S. G. Shaqfeh, Theory to predict particle migration and margination in the pressure-driven channel flow of blood, Phys. Rev. Fluids **2**, 093102 (2017).
[24] Q. M. Qi and E. S. G. Shaqfeh, Time-dependent particle migration and margination in the pressure-driven channel flow of blood, Phys. Rev. Fluids **3**, 034302 (2018).
[25] C. Bacher, A. Kihm, L. Schrack, L. Kaestner, M. W. Laschke, C. Wagner, and S. Gekle, Antimargination of microparticles and platelets in the vicinity of branching vessels, Biophys. J. **115**, 411 (2018).

[26] P. Perdikaris, L. Grinberg, and G. E. Karniadakis, Multiscale modeling and simulation of brain blood flow, Phys. Fluids **28**, 021304 (2016).
[27] D. A. Fedosov, M. Dao, G. E. Karniadakis, and S. Suresh, Computational biorheology of human blood flow in health and disease, Ann. Biomed. Engng. **42**, 368 (2014).
[28] A. Nacev, C. Beni, O. Bruno, and B. Shapiro, The behaviors of ferromagnetic nano-particles in and around blood vessels under applied magnetic fields, J. Magn. Magn. Mater. **323**, 651 (2011).
[29] J. B. Freund and B. Shapiro, Transport of particles by magnetic forces and cellular blood flow in a model microvessel, Phys. Fluids **24**, 051904 (2012).
[30] E. M. Cherry and J. K. Eaton, A comprehensive model of magnetic particle motion during magnetic drug targeting, Int. J. Multiphase Flow **59**, 173 (2014).
[31] Z. Li, Y. Zhu, R. R. Rao, J. R. Clausen, and C. K. Aidun, Nanoparticle transport in cellular blood flow, Comput. Fluids **172**, 609 (2018).
[32] H. Ye, Z. Shen, L. Yu, M. Wei, and Y. Li, Manipulating nanoparticle transport within blood flow through external forces: An exemplar of mechanics in nanomedicine, Proc. R. Soc. London, Ser. A **474**, 20170845 (2018).
[33] A. S. Popel and P. C. Johnson, Microcirculation and hemorheology, Annu. Rev. Fluid Mech. **37**, 43 (2005).
[34] T. W. Secomb, Blood flow in the microcirculation, Annu. Rev. Fluid Mech. **49**, 443 (2017).
[35] E. C. Eckstein and F. Belgacem, Model of platelet transport in flowing blood with drift and diffusion terms, Biophys. J. **60**, 53 (1991).
[36] D. Leighton and A. Acrivos, The shear-induced migration of particles in concentrated suspensions, J. Fluid Mech. **181**, 415 (1987).
[37] L. Crowl and A. L. Fogelson, Analysis of mechanisms for platelet near-wall excess under arterial blood flow conditions, J. Fluid Mech. **676**, 348 (2011).
[38] J. Li, M. Dao, C. T. Lim, and S. Suresh, Spectrin-level modeling of the cytoskeleton and optical tweezers stretching of the erythrocyte, Biophys. J. **88**, 3707 (2005).
[39] I. V. Pivkin and G. E. Karniadakis, Accurate Coarse-Grained Modeling of Red Blood Cells, Phys. Rev. Lett. **101**, 118105 (2008).
[40] K. I. Tsubota, C. Wada, and T. Yamaguchi, Simulation study on effects on hematocrit on blood flow properties using particle method, J. Biomech. Sci. Eng. **1**, 159 (2006).
[41] T. Wang, T.-W. Pan, Z. W. Xing, and R. Glowinski, Numerical simulation of rheology of red blood cell rouleaux in microchannels, Phys. Rev. E **79**, 041916 (2009).
[42] Y. Liu, L. Zhang, X. Wang, and W. K. Liu, Coupling of Navier-Stokes equations with protein molecular dynamics and its application to hemodynamics, Int. J. Numer. Methods Fluids **46**, 1237 (2004).
[43] R. Glowinski, T. W. Pan, T. I. Hesla, and D. D. Joseph, A distributed Lagrange multiplier/fictitious domain method for particulate flows, Int. J. Multiphase Flow **25**, 755 (1999).
[44] R. Glowinski, T. W. Pan, T. I. Hesla, D. D. Joseph, and J. Periaux, Distributed Lagrange multiplier/fictitious domain methods for flows around moving rigid bodies: Application to particulate flow, Int. J. Numer. Method Fluids **30**, 1043 (1999).
[45] R. Glowinski, T. W. Pan, T. I. Hesla, D. D. Joseph, and J. Periaux, A fictitious domain of incompressible viscous flow past moving rigid bodies: Application to particulate flow, J. Comput. Phys. **169**, 363 (2001).
[46] S. G. Yiantsios, On the distributed Lagrange multiplier/fictitious domain method for rigid-particle-laden flows: A proposition for an alternative formulation of the Lagrange multipliers, Int. J. Numer. Method Fluids **70**, 1027 (2012).
[47] P. Saliakellis and S. G. Yiantsios, Macroscopic characteristics of heavy particle resuspension obtained from direct numerical simulations of pressure driven channel flow, Int. J. Multiphase Flow **84**, 188 (2016).
[48] A. R. Pries, D. Neuhaus, and P. Gaehtgens, Blood viscosity in tube flow: Dependence on diameter and hematocrit, Am. J. Physiol. **263**, H1770 (1992).
[49] D. J. Jeffrey and Y. Onishi, The slow motion of a cylinder next to a plane wall, Quart. J. Appl. Math. Mech. **34**, 129 (1981).
[50] J. Happel and H. Brenner, *Low Reynolds Number Hydrodynamics*, 2nd ed. (Martinus Nijhoff Publishers, Dordrecht, 1986).

[51] A. S. Dvinsky and A. S. Popel, Motion of a rigid cylinder between parallel plates in Stokes flow: Part 1: Motion in a quiescent fluid and sedimentation, Comput. Fluids **15**, 391 (1987).
[52] P. R. Nott and J. F. Brady, Pressure-driven flow of suspensions: Simulation and theory, J. Fluid Mech. **275**, 157 (1994).
[53] R. M. Miller and J. F. Morris, Normal stress-driven migration and axial development in pressure-driven flow of concentrated suspensions, J. Non-Newtonian Fluid Mech. **135**, 149 (2006).
[54] P. Olla, The lift on a tank-treading ellipsoidal cell in a shear flow, J. Phys. II France **7**, 1533 (1997).
[55] I. Cantat and C. Misbah, Lift Force and Dynamical Unbinding of Adhering Vesicles under Shear Flow, Phys. Rev. Lett. **83**, 880 (1999).
[56] S. Sukumaran and U. Seifert, Influence of shear flow on vesicles near a wall: A numerical study, Phys. Rev. E **64**, 011916 (2001).
[57] M. Abkarian, C. Lartigue, and A. Viallat, Tank Treading and Unbinding of Deformable Vesicles in Shear Flow: Determination of the Lift Force, Phys Rev. Lett. **88**, 068103 (2002).
[58] N. Callens, C. Minetti, G. Coupier, M.-A. Mader, F. Dubois, C. Misbah, and T. Podgorski, Hydrodynamic lift of vesicles under shear flow in microgravity, Europhys. Lett. **83**, 24002 (2008).
[59] G. Coupier, B. Kaoui, T. Podgorski, and C. Misbah, Noninertial lateral migration of vesicles in bounded Poiseuille flow, Phys. Fluids, **20**, 111702 (2008).